Supplementary material - Preclinical imaging using single track location shear wave elastography: monitoring the progression of murine pancreatic tumor liver metastasis in vivo.

Rifat Ahmed, *student member, IEEE*, Jian Ye, Scott A. Gerber, David C. Linehan, Marvin M. Doyley *senior member, IEEE*

I. Understanding the effect of motion on STL-SWE estimates

Previous studies have reported the effect of physiological motion on the SWS estimates provided by MTL-SWE based methods [1]. These motion sources, however, impact STL-SWE differently than MTL-SWE. In MTL-SWE, often a push-detect ensemble is acquired with the help of ultrafast parallel beamforming strategies. Since the acquisition time of a single push-detect ensemble is significantly smaller (<20 ms) than a respiration or cardiac cycle, motion induced from these sources appears as a low frequency offset. Thus, standard Fourier domain filters are used to diminish their impacts. STL-SWE, on the other hand, inherently relies on multiple push-detect ensembles. Thus, the contribution of physiological motion in STL-SWE can be separated into two components: intra-push and inter-push motion. Intra-push motion is similar to MTL-SWE and can be mitigated by applying band-pass Fourier filters on the slow-time wave profiles (we performed this in this study). However, the inter-push motion can cause the push beams to register at unknown locations. Since in STL-SWE, the information of push locations is used in the SWS estimation process, the unknown registrations of push beams (and track beams) due to inter-push motion can potentially introduce unknown bias and variance. The goal of this section is to understand the impact of inter-push motion on STL-SWE using a theoretical analysis and under simple experimental conditions in phantoms.

Theoretical understanding

Fig S1a exhibits an STL-SWE pulse sequence with two push beams located at points A and B and operating without any external motion. The shear waves generated from these two pulses are tracked at a common point C which is x_1 and x_2 distances apart from the two beams, respectively. The points A, B, and C are defined in tissue coordinates. The true arrival times of the shear waves at the common location C are t_1 and t_2, respectively. Ultrasound beams are sensitive to the motion of the areas of constructive interference within the spatial sensitivity function [2]. Thus, the true effect of speckle is an inaccurate estimation of the location where the measured arrival time spatially registers. However, we can also think of the speckle-induced effects as an inaccurate estimate of the arrival time for the expected measuring location. The speckle induced errors in the estimates of the arrival times are e_1 and e_2 for the two push events, respectively. The SWS estimate, c_s, is given by

$$c_s = \frac{x_2 - x_1}{(t_2 + e_2) - (t_1 + e_1)}. \tag{1}$$

Due to use of a common tracking location, $e_1 = e_2$,

$$c_s = \frac{x_2 - x_1}{t_2 - t_1} = \frac{\Delta x}{\Delta t}. \tag{2}$$

Next, we assume that there is a rigid intra-push motion that displaces the positions of the push and track in the second event. Although actual tissue motion can displace the locations corresponding to both events, the analysis described here generalizes such scenarios. Additionally, we are ignoring inter-push motion since its contribution can often be diminished by post-processing filters. The displaced push and track locations in the second event are in D and E, respectively, in tissue coordinate. The configuration is illustrated in **Fig. S1b**. Although the illustration shows the second push event within the same field-of-view, the analysis can be generalized to arbitrary in-plane and out-of-plane motion. The true arrival time at the new location is t_3.The speckle-induced error in arrival time estimate associated with the new location is e_3, and it is different from e_1 or e_2. The SWS estimate, c_{s1}, obtained from this motion-corrupted dataset is given by

$$c_{s1} = \frac{x_3 - x_1}{(t_3 + e_3) - (t_1 + e_1)}. \tag{3}$$

Now, the distance x_3 is defined in transducer coordinates by the beamforming process and thus $x_3 = x_2$. Consequently,

$$c_{s1} = \frac{x_2 - x_1}{(t_3 + e_3) - (t_1 + e_1)}. \tag{4}$$

Additionally, if we are imaging an elastically homogeneous medium, the arrival times t_2 and t_1 are equal since they are associated with equal propagation path lengths in mediums with equal SWS. Thus,

$$c_{s1} = \frac{x_2 - x_1}{t_2 - t_1 + e} = \frac{\Delta x}{\Delta t + e} \tag{5}$$

where $e = e_3 - e_1$. Approximating in first order,

$$c_{s1} \approx \frac{\Delta x}{\Delta t} - \frac{e \Delta x}{(\Delta t)^2} \tag{6}$$

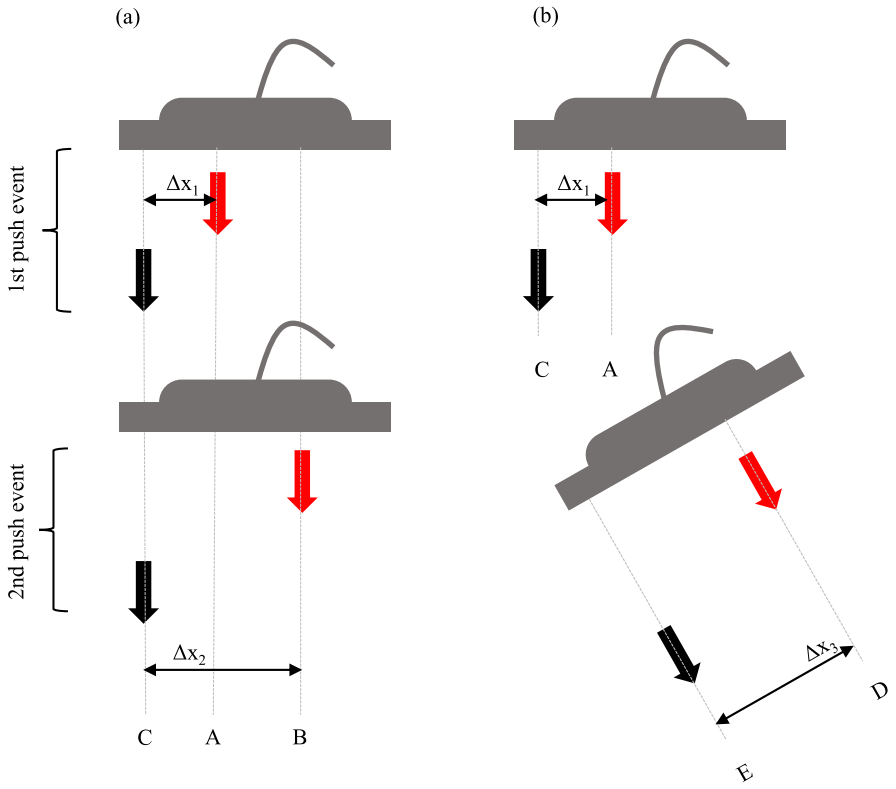

Fig. S1: Illustrates the relative positions of push and track locations for STL-SWE in tissue coordinates. Red and black vertical arrows represnt push and track beams, respectively. (a) shows the configuration in the absence of tissue motion using two push events. (b) shows the same conguration when inter-push motion has displaced the the push and track locations in the second event. In the transducer coordinate, however, the push and track positions remain unchanged despite the motion.

The estimate of c_{s1} approaches c_s when large Δx is used since the wave time delay in the second term will increase quadratically. The equation (5) and such dependence of bias are characteristic of MTL-SWE. Thus, inter-push motion effectively converts the acquired data to an MTL-SWE estimator. Consequently, irrespective of the magnitude or direction of inter-push motion in a homogeneous medium, the spatial mean of estimated SWS computed over a reasonably large ROI will exhibit no bias, although the variance will increase.

For heterogeneous materials, such analysis is difficult to perform. The true arrival time delay $t_3 - t_1$ in equation (5) will be different from $t_2 - t_1$ in such materials. Consequently, the estimate will exhibit bias. For an arbitrary and potentially out-of-plane inter-push motion, the difference between these two time delays depends on the SWS heterogeneity and the vector magnitude of the motion. Consequently, the bias may either be positive or negative at different pixels of the image.

Phantom experiment

We acquired STL-SWE data from a commercially available phantom (Model 06GSE, CIRS, Norfolk, VA) which has a homogeneous region and a cylindrical inclusion that is softer compared to the homogeneous background. For each phantom, we collected three sets of data sets at three static positions of the phantom. The transducer was mounted on an adjustable translation stage and the imaging was performed through water, enabling controlled movement of the transducer. After the first acquisition at a fixed position, we collected the second dataset at the same imaging cross-section. However, in between the two acquisitions, we moved the transducer down axially by 2 mm. The third acquisition was performed in a cross-section that is elevationally distant (~5 cm) from the location in the first two acquisitions while maintaining a fixed axial distance between transdcuer and phantom. Each acquisition at a given location was also repeated five times without moving the transducer to provide statistical power over subsequent analysis. This scheme was repeated on the inclusion phantoms. However, for the inclusion phantom, the third acquisition was performed at a homogeneous cross-section outside the inclusion region.

Data analysis

We used the three datasets acquired at three static cross-sections to simulate different conditions for inter-push motion. In STL-SWE, a column of SWS is reconstructed using two push ensembles. To simulate an axially upward intra-push motion, we constructed a dataset where, for any given column of SWS, the first push ensemble was taken from the corresponding ensemble in the first acquisition and the second ensemble was obtained from corresponding ensemble in the second dataset. Similarly, another dataset was constructed where the first push ensemble of a given SWS column

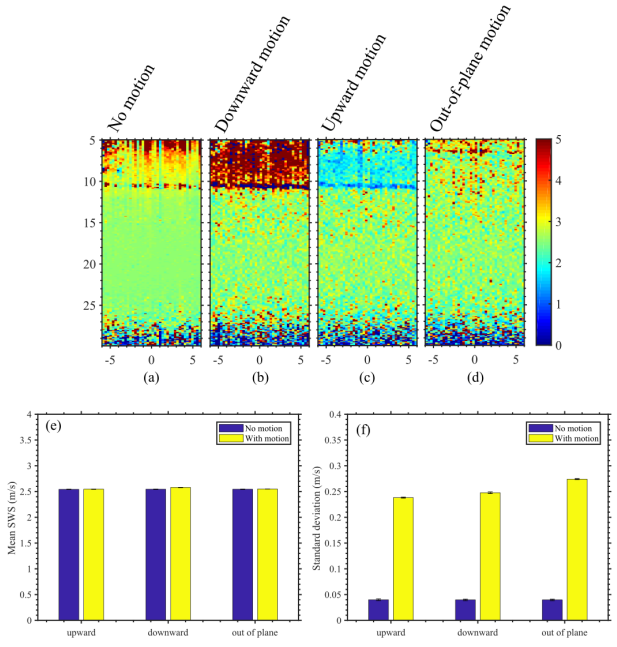

Fig. S2: Evaluating the impact of motion on STL-SWE elastograms using a homogeneus phantom. By collecting data at three different phantom positions, synthetic data was constructed with different types of motion. (a)-(d) shows elastograms when there is no motion, upward axial motion, downward axial motion and large out-of-plane motion, respectively. The top part of the images (5-10 mm) contained reverberating echo between the water layer and phantom and was excluded from the data interpretation. (e) Mean and (f) standard deviation of SWS calculated for different types of motion at 20 mm using a 5 mm axial kernel.

was obtained from the correspnding ensemble in the second acquisition and the second ensemble was taken from the corresponding ensemble in the first acquisition. This effectively simualted a condition for axially downward inter-push tissue motion. Similarly, we contructed a dataset by combinining the second and third acquisitions, which effectively simulated a condition for large elevational intra-push motion. These synthetically motion-corrupted datasets were processed to obtain SWS estimates. Additionally, we processed the motion-free original acquisitions to obtain a reference for comparison. For the homogeneous phantom, we evaluted mean and standard deviation for both types of datasets (motion-free and motion-corrupted) at 20 mm depth using a 5 mm axial ROI.

Results

For the homogeneous phatom, irrespective of the type of motion, the difference between the mean SWS of the motion-free and the motion-corrupted condition was up to 1.37%. However, the standard deviation was 495% to 589% higher in the motion-corrupted conditions compared to the corresponding motion-free conditions (**Fig. S2**). For the inclusion phantom, axial motion resulted in shape distortion of the inclusion (**Fig. S3**). Unlike the homogeneous phantom, motion resulted in biased estimates of SWS. A given pixel (pixels

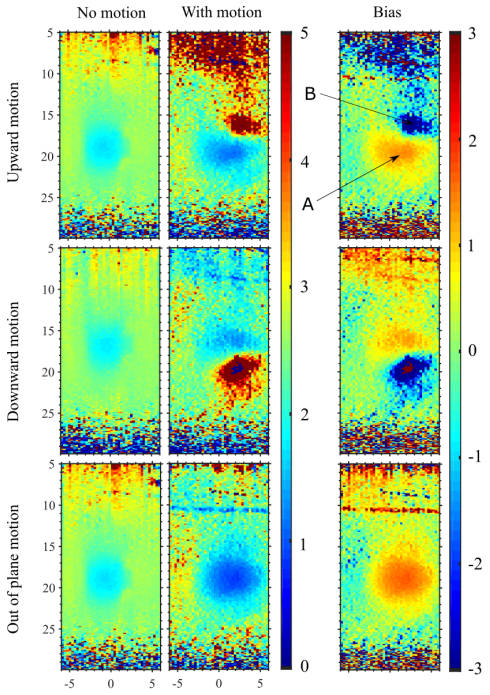

Fig. S3: Evaluating the impact of motion on STL-SWE elastograms using a soft inclusion phantom. By collecting data at three different phantom positions, synthetic data was constructed with different types of motion. The first, second and third rows correspond to conditions involving axially upward, axially downward and out of plane motion, respectively. First and second columns show elastograms when there is no motion and presence of motion in data, resepctively. The third column shows bias in the motion corrupted elastograms in a pixel-wise manner. Positive bias indicates an under estimation and negative bias indicates an overestimation. The bias images are a pixel-wise mean of five repeated acquisitions for a given configuration.

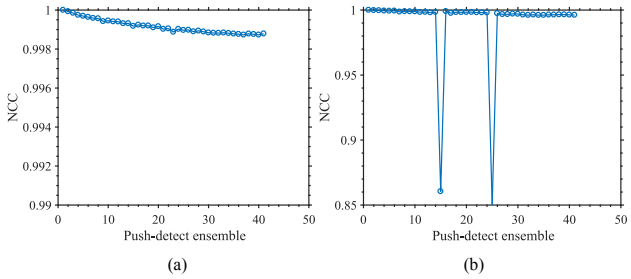

Fig. S4: Illustrating the presence or absence of motion in pSTL-SWE data obtained from a homogeneous phantom. The technique used in the computation of NCC profiles in Figure 4 was used here. (a) and (b) correspond to acquisitions in without motion and with externally applied motion, respectively. External motion was applied to the transducer during the acquisition of the 15^{th} and 25^{th} push-detect ensembles of the data corresponding to (b). Different ranges along the y-axis were used in these two plots to visualize the variations in NCC.

A or B in **Fig. S3**, for example), however, can either be overestimated or underestimated depending on the type of the motion.

Discussion

In the homogeneous materials, the intra-push motion in STL-SWE effectively converts the acquisition to an MTL-SWE acquisition. Even when the motion is so severe that the speckles are completely uncorrelated between a pair of ensembles, accurate (spatially) SWS is reconstructed albeit with higher spatial variance. For heterogeneous targets, on the other hand, there is both bias and variance in SWS reconstrution in the presence of motion. The nature of the bias (positive or negative), however, depends on the motion (magnitude and direction), the true SWS between the expected push-positions and the motion-corrupted push-positions, and true SWS in between the expected track-position and the motion-corrupted track-positions. This is practically consequential for clinical and preclinical applications. For clinical systems, quality indicators are implemented for SWE where the range of SWS values, the energy of the shear wave or the cross-correlation-coefficient of wave signals are often used to assess the fidelity of estimation [3]. The results presented here demonstrate that the SWS estimates obtained from the motion-corrupted data are often in the range expected in tissues or phantoms. Additionally, according to the theoretical analysis and experimental data presented here, the wave cross-correlation and wave energy may remain unperturbed. Thus, currently used quality indicators may not be able to detect the motion corruption in STL-SWE. The cross-correlation based analysis presented in **Fig 4** (in main paper) is an effective approach to achieve this goal.

For *in vivo* STL-SWE imaging, the task of estimating SWS bias created by motion is non-trivial. Due to inherent heterogeneity, the bias cannot be estimated spatially and must be evaluated per pixel. One experimental way to achieve this is by comparing motion-free and motion-corrupted acqusitions for a given pixel. However, one must replicate the motion in a repeatable manner (in regards to timing and location) to provide statistical power to the estimation. However, this is challenging due to practical considerations involving animals. Due to these challenges, we have qualitatively evaluted the impact of motion on *in vivo* SWS elastogram. Nevertheless, we have demonstrated that the presence of intra-push motion in the acquired data can be easily detected by performing cross-correlation on push-detect data.

II. Detecting tissue motion in STL-SWE data

We have demonstrated (**Fig 4** in the main manuscript) that the presence of tissue motion can be detected by performing cross-correlation analysis on the acquired data. In this section, we demonstrate the nature of the cross-correlation profile in the absence and presence of motion under controlled experimental conditions using a homogeneous phantom. We used the homogeneous phantom described in the previous section.

First, we collected a pSTL-SWE dataset without any external motion from the homogeneous phantom. Despite no external motion, from one push-detect ensemble to the next there is a difference in the push-location, which creates a difference in shear wave motion. This effectively resulted in a reduced correlation between tracking frames of the two push-detect ensembles. Additionally, the tracking frames from the first push-detect ensemble was used as a reference in the cross-correlation. When tracking frames from gradually distant push-detect ensembles were cross-correlatd with this reference, the push beam location between these ensembles also increased. This effectively resulted in a gradual decay in NCC even when there was no external motion.

We collected a second pSTL-SWE on the same cross-section of the phantom. In this case, the pulse sequence in the Verasonics research scanner was modified to display a text before the initiation of a push-detect ensemble. Using this text-display as a timing reference, a momentary downward external pressure was applied to the transducer during the acquisition of 15^{th} and 25^{th} push-detect ensemble. **Figure S4** indicates that large drops in NCC are observable during these push-detect events. Although there is an inherent decay in NCC due to the shear wave motion, external motion that is larger than shear wave amplitudes can be identified from these NCC profiles using standard outlier detection methods.

III. Supplementary tables

TABLE S1: Details of imaging parameters used in all studies.

Parameter	Value (Unit)
Push frequency	5 MHz
Track frequency	10 MHz
Push F#	2.0
Tracking PRF	12 KHz
Push and tracking voltage	42 V
Tracking plane wave angles	-1°, 0°, 1°
Number of push locations	41
Push spacing	0.3 mm
Transducer	L11-5v
Transducer pitch	0.3 mm
Time between rapid focal pushes	10 µs
Duration of single focal push	150 µs
Number of rapid focal zones	4

References

[1] D. M. Giannantonio, D. M. Dumont, G. E. Trahey, and B. C. Byram, "Comparison of physiological motion filters for in vivo cardiac ARFI," *Ultrasonic Imaging*, vol. 33, no. 2, pp. 89–108, apr 2011.

[2] S. A. McAleavey, L. O. Osapoetra, and J. Langdon, "Shear wave arrival time estimates correlate with local speckle pattern," *IEEE transactions on ultrasonics, ferroelectrics, and frequency control*, vol. 62, no. 12, pp. 2054–2067, 2015.

[3] T. Deffieux, J.-L. Gennisson, B. Larrat, M. Fink, and M. Tanter, "The variance of quantitative estimates in shear wave imaging: Theory and experiments," *IEEE Transactions on Ultrasonics, Ferroelectrics and Frequency Control*, vol. 59, no. 11, p. nil, 2012. [Online]. Available: https://doi.org/10.1109/tuffc.2012.2472